Design of an Inductive Spiral-Loop Loaded Unit Cell in a Mushroom-Shaped High Impedance Surface for Sub-GHz Applications

Sungcheol Hong[‡], Woo Seok Kim[‡], and Sung Il Park[*]

Abstract—A high impedance surface has far-reaching potential in wireless applications, but realization of the surface operating at sub-GHz ranges is challenging due to its size limits in practical applications. Here, we present a novel inductive technique based on multi-turn square spiral loops. The introduction of the spiral loops to a mushroom-shaped high impedance surface provides additional current path, thereby results in a dramatic increase in its total inductance at given dimensions, and therefore leads to a significant reduction in a resonant frequency of a high impedance plane. Electromagnetic simulation results reveal that a resonant frequency shifts downward 1 GHz at a given dimension, and they are in good agreement with results from an analytical model for the proposed structure. Experimental measurements suggest the feasibility of the proposed approach.

1. INTRODUCTION

A mushroom-shaped high impedance surface (HIS) is a periodic structure, and each of its unit cells is composed of a protuberant metallic patch and a ground plane which are linked to each other through a conductive via [1, 2]. When electromagnetic wave is incident upon its periodic metallic surfaces, the gap between the neighboring patches provides capacitance whereas the vias provide inductance. With the condition that the period of the unit cell is much smaller than the operating wavelength, the HIS simply behaves as a parallel resonant LC filter circuit blocking the flow of currents along its surface and consequently can suppress surface wave. Another interesting characteristic is that while a perfect conductor generates a 180-degree phase shift of reflected electromagnetic wave, the HIS generates 0-degree phase shift. Thus, it acts as a hypothetical perfect magnetic conductor and forms constructive interference between incident and reflected waves.

The above two benefits have been widely utilized in several practical applications. In the area of antenna designs [3–7], HISs have been utilized to develop low-profile and high-gain antennas. In principle, the distance between the radiating element and the ground plane of a printed antenna such as a microstrip antenna should be quarter wavelength. If the distance is reduced under this limitation, surface wave, distorting the radiation pattern and reducing the antenna gain, is formed around the antenna. However, when a HIS is located beneath a low-profile antenna, the thickness restriction of a printed antenna can be alleviated because it efficiently suppresses surface wave flowing around the antenna. Furthermore, when wave, radiating in backward direction of an antenna, is incident upon a HIS, it reflects the wave with zero-degree shift. This results in constructive interference between the radiated wave from the antenna and the reflected wave from the HIS and ultimately enhances the antenna gain. Interestingly, the characteristic of zero-degree phase shift was also used in wireless power transmission. In [8], inductive coupling coils were located on the upper side of a HIS, and transmission

efficiency was prominently enhanced by constructive magnetic field interference. This suggests related opportunities for applications of implantable wireless electronics in biomedical fields [9–11].

Although HISs have some utilities, their full potentials are not reached in sub-GHz applications. Implementation of sub-GHz HISs operating at the given dimensions comparable with portable devices would not be feasible because of the considerably increased sizes of their unit cells. To tackle this problem, several researchers have focused on techniques to decrease the resonant frequencies of HISs by increasing their capacitance or inductance. In [12], high capacitance was obtained by utilizing double-layered hexagonal metal patches, and Durgun et al. proposed a perforated ground plane to obtain extra inductance [13]. However, these two approaches have drawbacks that the double-layered hexagonal metal patches would increase the overall thickness, and a perforated ground plane would form undesired radiation like a slot antenna. Moreover, reductions in resonant frequency of their structures are modest. In [14], we proposed a new approach, inductive loading, employing a 3-D inductor. Here, a long single via is replaced by short multiple sub-vias, and thereby current paths are extended. This results in 27% reduction in the resonant frequency of a mushroom-shaped HIS significantly without increasing its thickness.

In this paper, we propose a new inductive loading approach using a square-shaped spiral loop inductor (SSLL). As shown in Figure 1, a multi-turn SSLL is additionally inserted between sub vias. Simulated and experimental results reveal that the insertion of SSLL leads to a dramatic downward shift in the resonant frequency (the three-layered HIS [14]: 3.69 GHz, the proposed structure: 1.36 GHz) at given dimensions (5 mm by 5 mm). Here, we also provide an analytical model of the proposed HIS, and it is in good agreement with a numerical approach.

<div align="center">(a)   (b)   (c)</div>
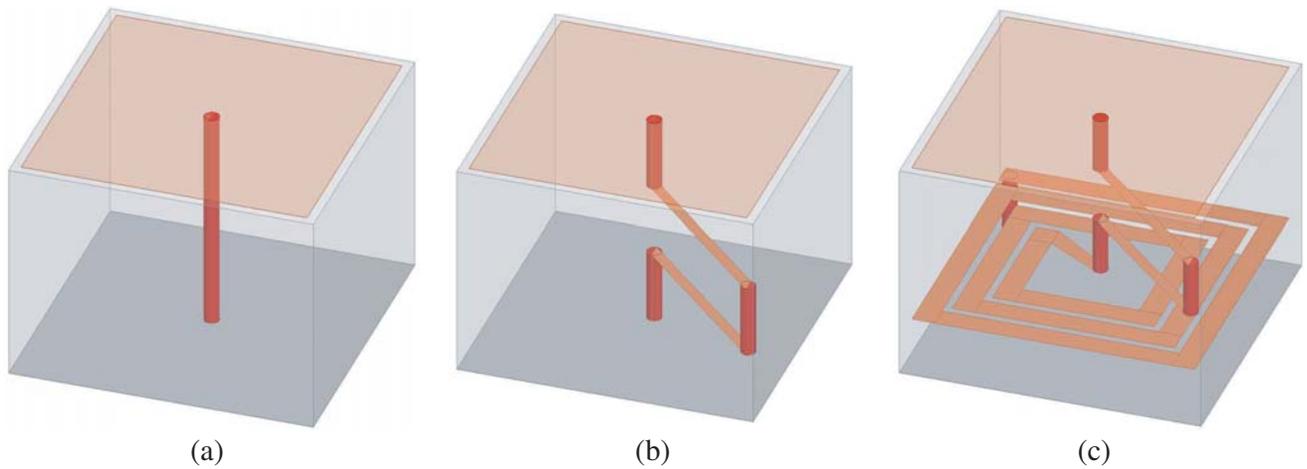
Figure 1. Perspective views of the unit cells in (a) a conventional, (b) the three-layered [14], and (c) the proposed HISs.

2. ANALYTICAL MODEL

As seen in Figure 2, the unit cell of our structure consists of a metallic patch, a ground plane, sub vias, extended current paths, substrates, and an SSLL. Coupling in the space between the adjacent patches leads to capacitance (0.35 pF), and the capacitance can be calculated by using the following formula [15].

$$C_u = \frac{(P - g)\,\epsilon_0\,(1 + \epsilon_r)}{\pi} \cosh^{-1}\left(\frac{2P - g}{g}\right). \tag{1}$$

Here, $\epsilon_0 = 8.854 \times 10^{-12}\,[\text{F·m}^{-1}]$ is the absolute permittivity, and ϵ_r is the relative dielectric constant of the substrate. As illustrated in Figure 3(a), an induced electrical current circulates around the top metallic patches, sub vias, extended current paths, SSLLs, and a ground plane, each of which can be modeled a discrete inductor with inductance of L_1, L_s, and L_p, respectively. Here, we use the modified

(a)

(b)

(c)
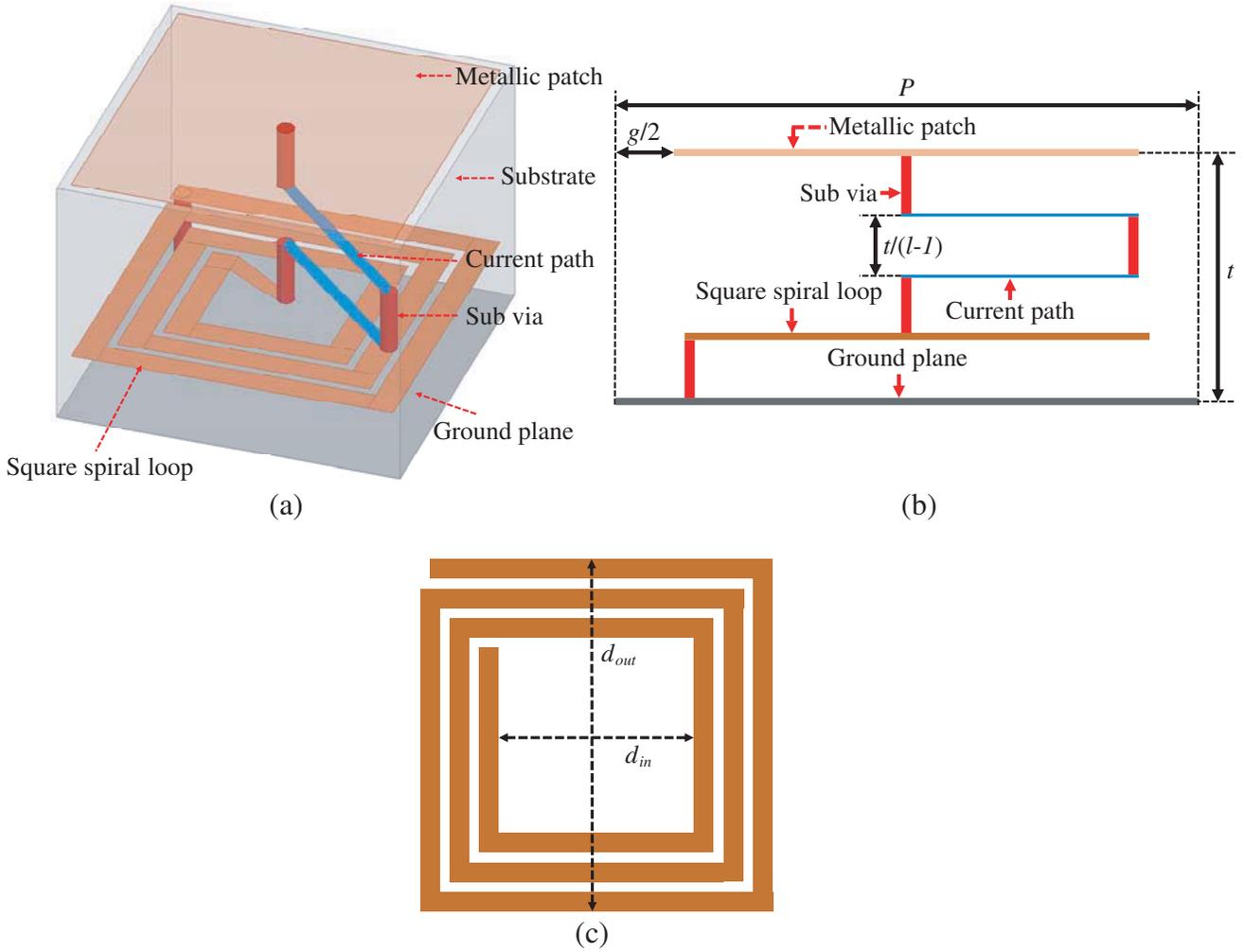
Figure 2. (a) Perspective and (b) cross-sectional view of the proposed HISs, respectively. (c) Top view of a square spiral loop with multi-turns.

(a)

(b)
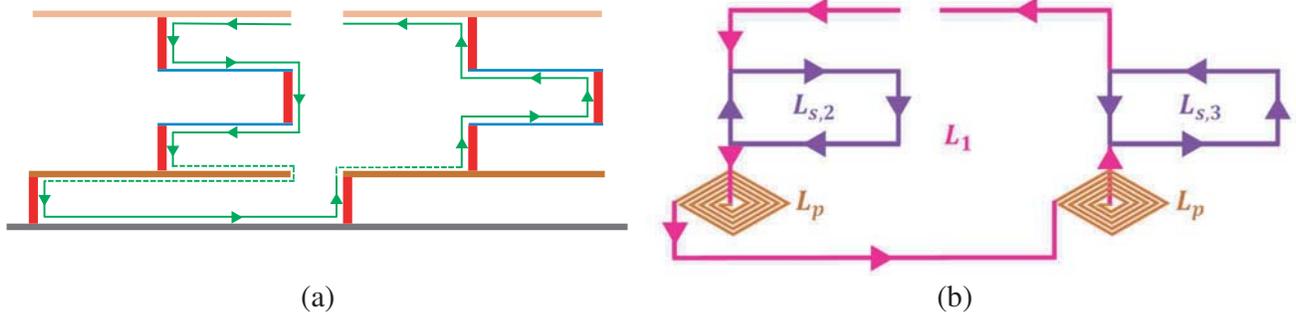
Figure 3. (a) Illustration of electrical current paths formed by adjacent unit cells and (b) an equivalent circuit model.

wheeler formula for L_p [16], and the mutual inductance from the pairs of L_s and L_p is ignored due to their opposite current directions. The followings are equations for each inductor.

$$L_1 = \mu_0 t \tag{2a}$$

$$L_s = \mu_0 \frac{\left(\dfrac{P-g}{2}\right)\dfrac{t}{(l+1)}}{P} \tag{2b}$$

$$L_p = 31.33\mu_0 n^2 \times \frac{a^2}{8a + 11c} \tag{2c}$$

$$L_u = L_1 + L_s + L_p \tag{2d}$$

where $\mu_0 = 4\pi \times 10^{-7}\,[\text{H·m}^{-1}]$ is the absolute permeability, l the number of the sub vias, $a = (d_{out} + d_{in})/4$, $c = (d_{out} - d_{in})/2$, and n the number of turns. Other geometric parameters are described in Figures 3(b) and (c). A HIS can be modeled to a simple parallel LC network, and we can calculate the resonant frequency by using the simple circuit formula,

$$f_0 = \frac{1}{2\pi\sqrt{L_u C_u}} \tag{3}$$

3. SIMULATION RESULTS

We perform full-wave simulations using a commercial finite element analysis software, HFSS, to verify the proposed design. Each unit cell has dimensions of 5 mm by 5 mm, and spacing between adjacent unit cells is 0.2 mm. As shown in Figure 4, two inner FR-4 substrates (0.024 inches thickness, $\epsilon_r = 4.4$) are sandwiched between two outer FR-4 substrates (0.039 inches thickness, $\epsilon_r = 4.4$), and three epoxy adhesives (0.0075 inches thickness, $\epsilon_r = 4.3$) are inserted between the substrates. The diameter of the vias and the width of the extended paths are 120 μm and 240 μm, respectively.

Here, we use the eigenmode analysis (Optimetrics package) with a side periodic boundary condition including a 19 cm away perfect matched layer that leads to dispersion diagrams where wave-vectors of k_x and k_y are swept along the path Γ to X band, X to M band, and M to Γ band of the irreducible Brillouin zone [17]. For plots of the diagrams from Γ to X band, the phase between the first pair of the boundary conditions is set to zero, and the phase between the second pair is varied from 0° to 180° with an increment of 15°. For plots of the diagrams from X to M band, the phase between the second pair is

(a)

(b)

(c)

(d)
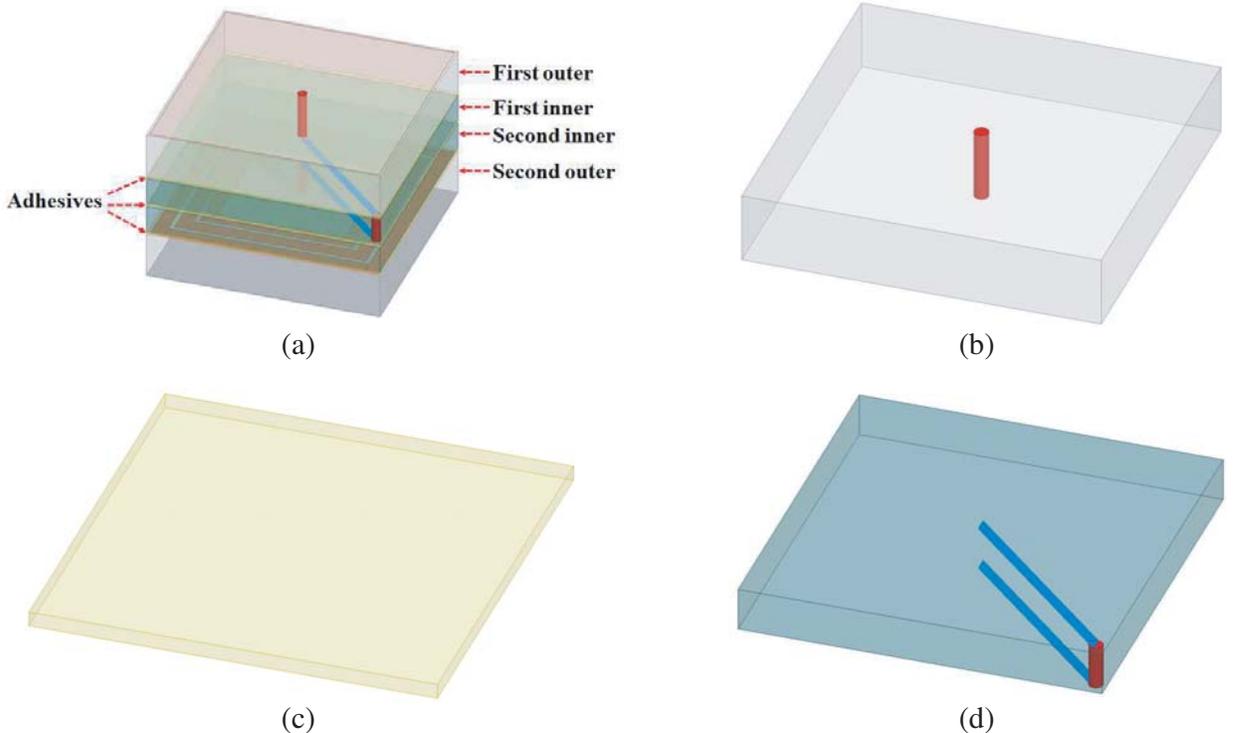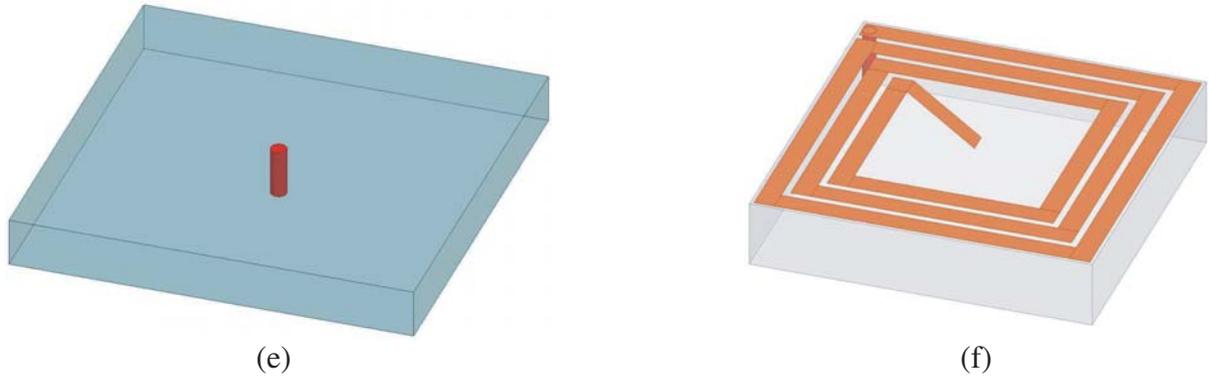
Figure 4. Illustrations of the proposed HIS in numerical simulations. (a) Perspective view, (b) first outer substrate, (c) adhesives, (d) first inner substrate, (e) second inner substrate, and (f) second outer substrate of its unit cell.
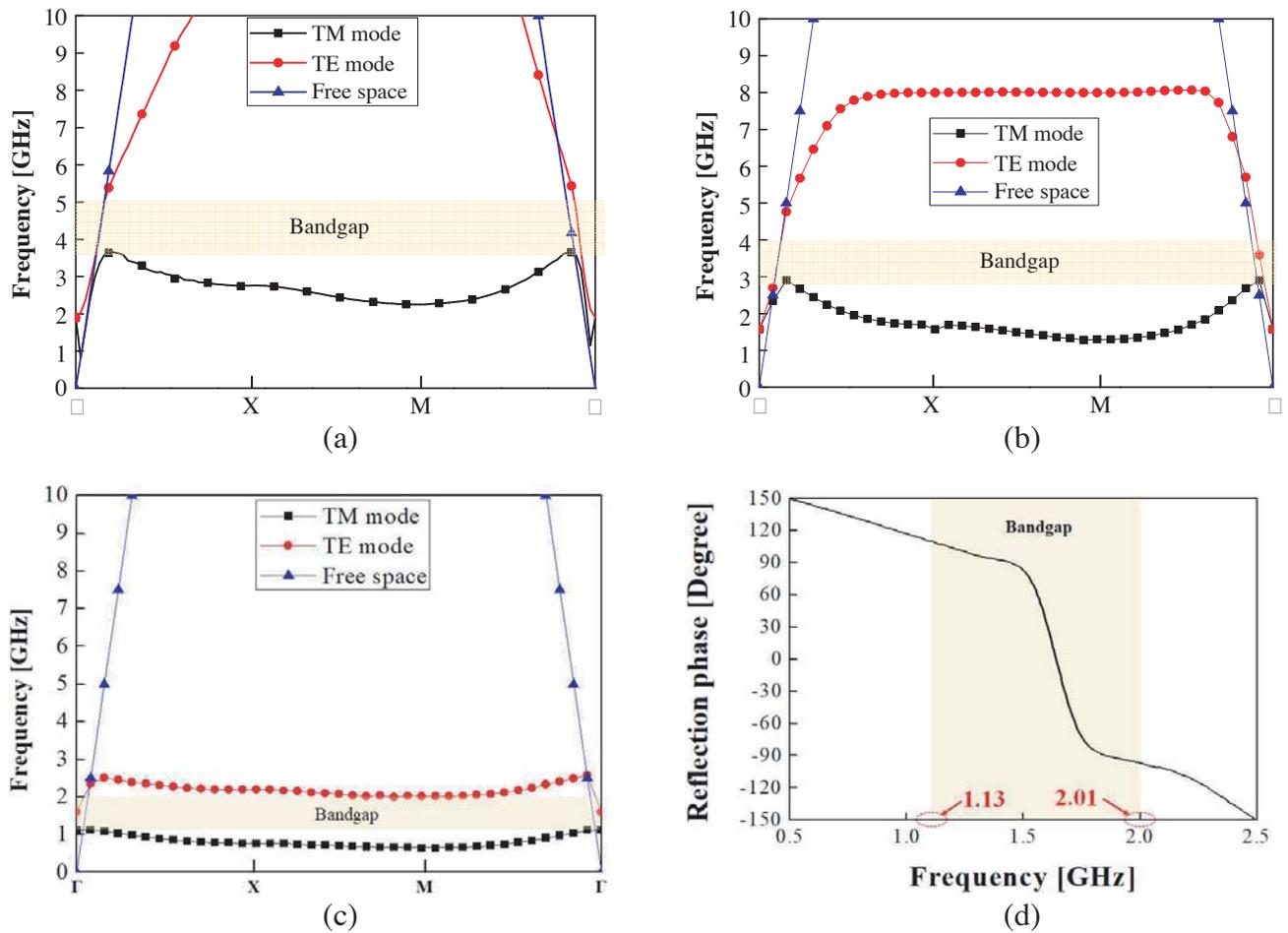
Figure 5. The 2D dispersion diagrams of the (a) conventional, (b) three-layered, and (c) proposed HIS. (d) The reflection phase of the proposed HIS.

fixed to 180° while the phase between the first pair is altered from 0° to 180° with the same increment. For M to Γ band, the two pairs are simultaneously changed from 180° to 0°.

The dispersion diagrams for the conventional, three-layered, and proposed HISs appear in Figure 5.

It shows the relation between wave vectors and frequency of surface waves, and we can determine the bandgap from the diagrams. Here, the bandgap is defined as a range of frequency where transverse magnetic (TM) and transverse electric (TE) waves are suppressed. These simulation results reveal that the proposed structure leads to a dramatic reduction (2.8 GHz; 66 %) in the resonant frequency compared with conventional (4.33 GHz) and three-layered structure (3.47 GHz). Here, the resonant frequencies are determined by the middle point of the bandgap. It also offers reasonably wide bandwidth (0.88 GHz).

   The aforementioned bandgap and resonant frequency are also observed from the reflection phase of the proposed HIS in Figure 5(d). As shown, the reflection phase is zero at the resonant frequency (1.57 GHz), and plane waves are approximately reflected in-phase inside the bandgap region. Additionally, we examined the effect of the epoxy adhesives in the proposed HIS. As shown in Figure 6, effects of the adhesive on suppression of surface waves are negligible. Table 2 summarizes the results of resonant frequency calculations from analytical and numerical approaches. The resonant frequencies in the analytical approach are obtained with the parameters given in Table 1. As expected, the proposed analytical model is consistent with a numerical approach. 10.5% discrepancy is due to parasitic capacitances associated with couplings between elements including adjacent extended paths, SSLLs, ground planes, and metallic patches.
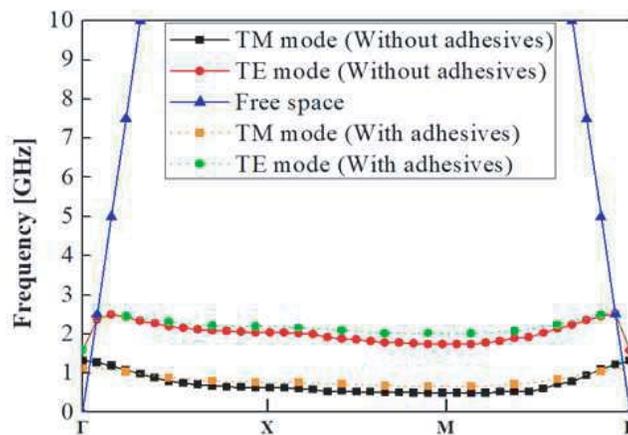
Figure 6. The effect of the epoxy adhesives in the proposed design.

Table 1. Summary of the geometrical parameters for the proposed design.

	P	g	t	l	ϵ_r	d_{out}	d_{in}
Values [mm]	5	0.2	3.2	3	4.4	4.8	0.56

Table 2. Summary of the resonant frequencies resulted from the analytical and numerical approaches.

	Approach	Conventional	Three-layered	Proposed [n = 3]
Resonant frequency [GHz]	Analytical	4.07	3.84	1.69
	Numerical	4.33	3.47	1.57

4. EXPERIMENT RESULTS

We fabricated the proposed HIS through one of the standard printed circuit board manufacturers (Royal Circuit Solutions). It has 16×16 unit cells, each of which has dimensions of 5 mm by 5 mm with a spacing of 0.2 mm between adjacent unit cells. The HIS consists of two outer FR-4 substrates (0.039

inches thickness, $\epsilon_r = 4.4$), two inner FR-4 substrates (0.024 inches thickness, $\epsilon_r = 4.4$), and B-stage epoxy films (0.0075 inches thickness, $\epsilon_r = 4.3$) as substrate adhesives. Blind micro vias with a diameter of 120 μm are drilled in the outer layers, and buried vias with a diameter of 120 μm are drilled in the inner layers. The width of extended paths on both sides of the first inner layer from the top surface is 240 μm.

An experimental setup for measurements of TM & TE waves appears in Figure 7(a). Here, a microwave absorber attached to its backside minimizes any radiation from the edge of the HIS that is not desirable. An Agilent E5062A network analyzer is connected to vertical and parallel pairs of the probe antennas to measure transmission coefficients of TM and TE waves propagating from the left end to the right end of the surface. Due to the nature of TM and TE surface waves, measurements of each wave require a different measurement setup [1, 14]. In TM propagation, the electric field extends vertically out of the surface, and measurements of TM waves require a pair of monopole antennas normal to the surface, as shown in Figure 7(b). Here, the vertical electric field of the antenna couples to the vertical field of the TM surface waves. In TE propagation, the electric field is parallel to the surface, and a pair of small monopole probes parallel to the sheet as shown in Figure 7(c) can measure TE waves. Figure 8 presents measurements of TM and TE wave transmission coefficients for both structures, the three-layered [14] and proposed HISs. Experiment results reveal that the insertion of a spiral loop leads to a significant reduction in the resonant frequency from 3.69 GHz to 1.36 GHz.

(a)

(b)

(c)
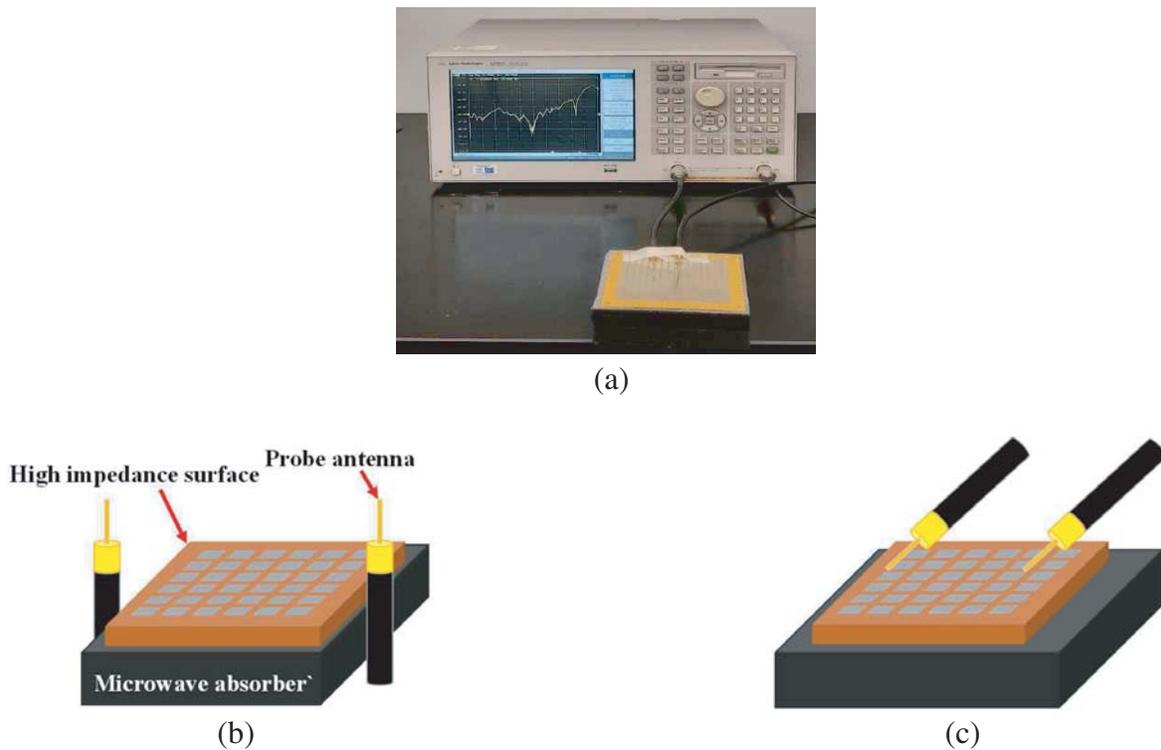
Figure 7. (a) Prospective view of the measurement setup. (b) TM and (c) TE surface wave transmission measurement approaches.

To determine the utility of the proposed structure in RFID applications, we conduct an experiment where antenna gain enhancement with the HIS is measured. Here, we use two UHF loop antennas (900 MHz) as shown in Figure 9(a). One of the antennas is positioned over the HIS and connected to port 1 of an Agilent E5062A network analyzer (VNA). The other loop antenna connected to port 2 of VNA is separated by a distance of 32 mm from it. Figure 9(b) shows the measured transmission coefficients between the antennas with and without the HIS. As seen, the field transmission is enhanced because of the increased antenna gain by the HIS. This suggests that the proposed HIS can boost
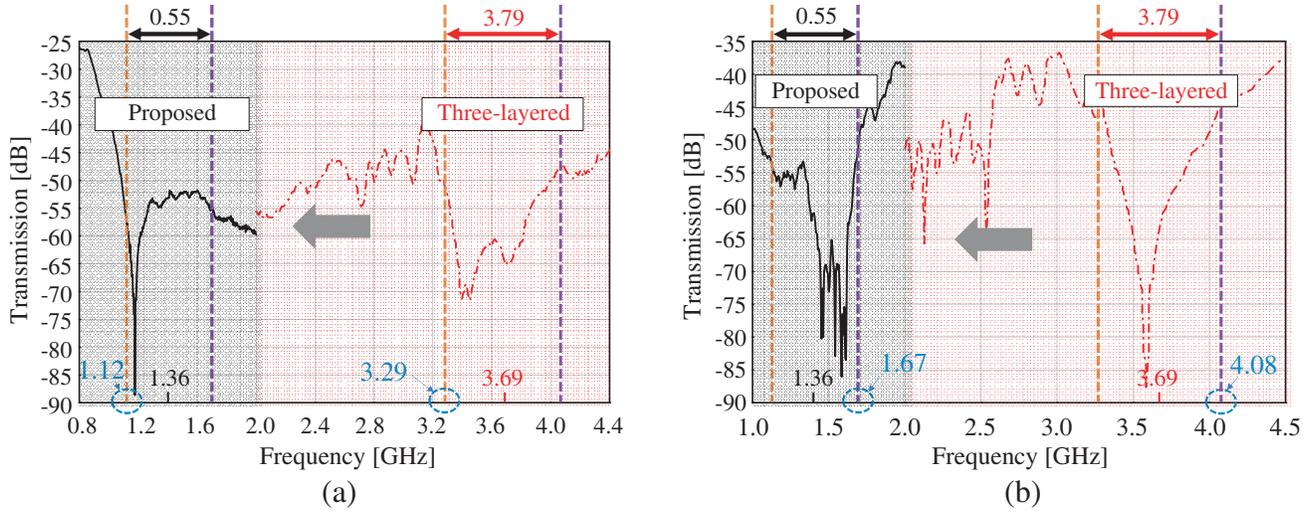
Figure 8. Plots of (a) TM and (b) TE wave transmission coefficients for the three-layer and proposed HISs. Here, the orange-dotted and violet-dotted lines indicate lower and upper limit of TM and TE waves, respectively.
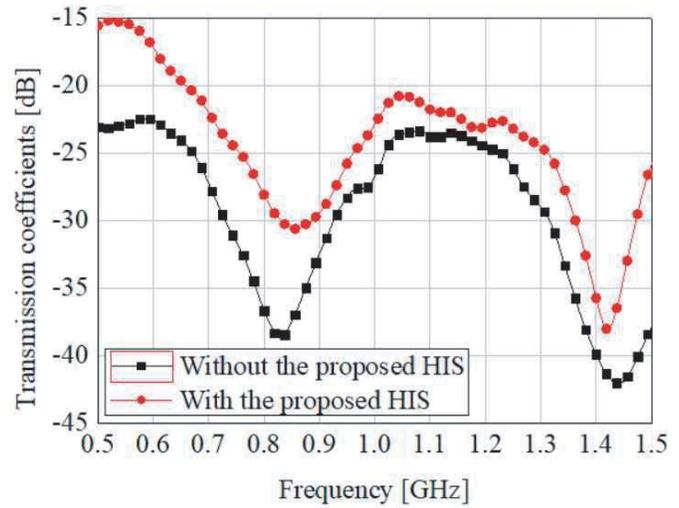
Figure 9. (a) Near-field loop antennas for 900 MHz RFID. (b) Measured transmission coefficients between the loop antennas with and without the proposed HIS.

transmission efficiency of UHF RFID systems and provides the potential for the widespread use of this technology in wireless data transmission or related fields.

5. DISCUSSION

In sub-GHz range conventional mushroom structures, the dimensions of their unit cells must be larger than 5 mm×5 mm. Otherwise, they would work at the above tens of GHz due to their low inductance and capacitance. The proposed inductive loading approach ensures high inductance at a given dimension, and thereby the dimensions of their unit cells and/or whole structures can be further reduced. This also suggests that more unit arrays can be incorporated, indicating that the full potential of HISs can be reached. For example, Table 3 summarizes comparisons of the proposed design with other approaches in

Table 3. Summary of the dimensions and the resonant frequencies of HISs.

No	Dimension of Unit cell	Resonant frequency
[1]	$0.112\lambda_0$	14 GHz
[23]	$0.054\lambda_0$	8.14 GHz
Three-layered	$0.057\lambda_0$	3.69 GHz
Proposed	$0.028\lambda_0$	1.36 GHz

terms of dimensions of a unit cell and corresponding resonant frequency. This suggests that a significant size reduction can be made by the adoption of the proposed approach to the HIS. We could establish the relationship between the size of the unit cell in a HIS and corresponding inductance of an SSLL embedded in it. This will set the upper and lower limits on the ranges of the resonant frequency at the given dimensions of the unit cell. Collectively, it will establish an effective range of guidelines for design, optimization, and fabrication of HISs with the novel inductive loading.

The proposed structure can be extended to the design having multi-layered SSLLs. It will lengthen current paths additionally and allow further reduction in the resonant frequency of a HIS. However, coupling that occurs between the SSLLs would also add parasitic capacitance to the structure, and the reduction of resonant frequency would be marginal. Here, the key to maximum shift in the resonant frequency is minimizing the electric coupling. This can be accomplished by interdigitated spiral loops [18]. Here, each of them has less turns, and traces on one loop are not aligned with those of another loop in the z direction. This results in reduced coupling between two SSLLs and therefore maximizes reduction in the resonant frequency of a HIS.

A key to the reduction in the resonant frequency of a HIS is the realization of high inductance at the given dimension. Fractal geometries would also be employed to achieve high inductance for a HIS [19, 20]. For example, a fractal loop inductor has considerable long electrical traces because of its a mathematical fractal pattern [21, 22]. Thus, without significant increase of its dimensions, the fractal loop inductor can provide much higher inductance than the previous multi-turn SSLL. Another embodiment of the fractal geometry is to employ fractal-patterned sub vias. Although these convoluted sub vias would cause parasitic couplings, it can yield significant high inductance at an optimization setting.

6. CONCLUSION

We proposed a novel scheme to lower the resonant frequency of a mushroom-shaped high impedance surface, which can be potentially utilized in sub-GHz wireless applications. The lowering of the resonant frequency is due to an increase in the inductance of a unit cell, associated with the additional three-dimensional inductor and spiral loop with n turns introduced. An analytical model establishes an effective range of guidelines for implementation of HIS operating at frequencies of interest. The proposed structure provides the potential for the widespread use of this technology in wireless communication or wireless power transmission.

REFERENCES

1. Sievenpiper, D., L. Zhang, R. F. Broas, N. G. Alexopolous, and E. Yablonovitch, "High-impedance electromagnetic surfaces with a forbidden frequency band," *IEEE Transactions on Microwave Theory and Techniques*, Vol. 47, No. 11, 2059–2074, 1999.

2. Clavijo, S., R. E. Diaz, and W. E. McKinzie, "Design methodology for Sievenpiper high-impedance surfaces: An artificial magnetic conductor for positive gain electrically small antennas," *IEEE Transactions on Antennas and Propagation*, Vol. 51, No. 10, 2678–2690, 2003.

3. Coccioli, R., F.-R. Yang, K.-P. Ma, and T. Itoh, "Aperture-coupled patch antenna on UC-PBG substrate," *IEEE Transactions on Microwave Theory and Techniques*, Vol. 47, No. 11, 2123–2130, 1999.

4. Vallecchi, A., J. R. De Luis, F. Capolino, and F. De Flaviis, "Low profile fully planar folded dipole antenna on a high impedance surface," *IEEE Transactions on Antennas and Propagation*, Vol. 60, No. 1, 51–62, 2011.

5. Kim, I. K., H. Wang, S. J. Weiss, and V. V. Varadan, "Embedded wideband metaresonator antenna on a high-impedance ground plane for vehicular applications," *IEEE Transactions on Vehicular Technology*, Vol. 61, No. 4, 1665–1672, 2012.

6. Mohamed-Hicho, N. M., E. Antonino-Daviu, M. Cabedo-Fabrés, and M. Ferrando-Bataller, "A novel low-profile high-gain UHF antenna using high-impedance surfaces," *IEEE Antennas and Wireless Propagation Letters*, Vol. 14, 1014–1017, 2015.

7. Wu, T., J. Chen, and P.-F. Wu, "Multi-mode high-gain antenna array loaded with high impedance surface," *IEEE Access*, Vol. 8, 147070–147076, 2020.

8. Park, S. I., "Enhancement of wireless power transmission into biological tissues using a high surface impedance ground plane," *Progress In Electromagnetics Research*, Vol. 135, 123–136, 2013.

9. Zhang, Y., D. C. Castro, Y. Han, Y. Wu, H. Guo, Z. Weng, Y. Xue, J. Ausra, X. Wang, R. Li, G. Wu, A. V. Guardado, Y. Xie, Z. Xie, D. Ostojich, D. Peng, R. Sun, B. Wang, Y. Yu, J. P. Leshock, S. Qu, C.-J. Su, W. Shen, T. Hang, A. Banks, Y. Huang, J. Radulovic, P. Gutruf, M. R. Bruchas, and J. A. Rogers, "Battery-free, lightweight, injectable microsystem for in vivo wireless pharmacology and optogenetics," *Proceedings of the National Academy of Sciences of the United States of America*, Vol. 116, No. 3, 21427–21437, 2019.

10. Zhang, H., P. Gutruf, K. Meacham, M. C. Montana, X. Zhao, A. M. Chiarelli, A. V. Guardado, A. Norris, L. Lu, Q. Guo, C. Xu, Y. Wu, H. Zhao, X. Ning, W. Bai, I. Kandela, C. R. Haney, D. Chanda, R. W. Gereau, IV, and J. A. Rogers, "Wireless, battery-free optoelectronic systems as subdermal implants for local tissue oximetry," *Science Advances*, Vol. 5, No. 3, 2019.

11. Kim, W. S., M. Jeong, S. Hong, B. Lim, and S.-I. Park, "Fully implantable low-power high frequency range optoelectronic devices for dual-channel modulation in the brain," *Multidisciplinary Digital Publishing Institute Sensors*, Vol. 20, 3639–3653, 2020.

12. Broas, R. F. J., D. F. Sievenpiper, and E. Yablonovitch, "A high-impedance ground plane applied to a cellphone handset geometry," *IEEE Transactions on Microwave Theory and Techniques*, Vol. 49, No. 7, 1262–1265, 2001.

13. Durgun, A. C., C. A. Balanis, C. R. Birtcher, H. Huang, and H. Yu, "High-impedance surfaces with periodically perforated ground planes," *IEEE Transactions on Antennas and Propagation*, Vol. 62, No. 9, 4510–4517, 2014.

14. Gu, M., D. Vorobiev, W. S. Kim, H.-T. Chien, H.-M. Woo, S. C. Hong, and S. I. Park, "A novel approach using an inductive loading to lower the resonant frequency of a mushroom-shaped high impedance surface," *Progress In Electromagnetics Research M*, Vol. 90, 19–26, 2020.

15. Bansal, A., B. C. Paul, and K. Roy, "An analytical fringe capacitance model for interconnects using conformal mapping," *IEEE Transactions on Computer-Aided Design of Integrated Circuits and Systems*, Vol. 25, No. 12, 2765–2774, 2006.

16. Wheeler, H. A., "Simple inductance formulas for radio coils," *Proceedings of the Institute of Radio Engineers*, 1398–1400, 1928.

17. Kovacs, P., "Design and optimization of electromagnetic band gap structures," Doctoral thesis in Brno University of Technology, 2010.

18. Zheng, S. F., Y. Z. Yin, H. L. Zheng, Z. Y. Liu, and A. F. Sun, "Convoluted and interdigitated hexagon loop unit cells for frequency selective surfaces," *Electronics Letters*, Vol. 47, No. 4, 233–235, 2011.

19. Bao, X. L., G. Ruvio, M. J. Ammann, and M. John, "A novel GPS patch antenna on a fractal hi-impedance surface substrate," *IEEE Antennas and Wireless Propagation Letters*, Vol. 5, 323–326, 2006.

20. Anwar, R. S., Y. Wei, L. Mao, and H. Ning, "Miniaturised frequency selective surface based on fractal arrays with square slots for enhanced bandwidth," *IET Microwaves, Antennas & Propagation*, Vol. 13, No. 11, 1811–1819, 2019.

21. Lazarus, N., C. D. Meyer, and S. S. Bedair, "Fractal inductors," *IEEE Transactions on Magnetics*, Vol. 50, No. 4, 2014.

22. Shoute, G. and D. W. Barlage, "Fractal loop inductors," *IEEE Transactions on Magnetics*, Vol. 51, No. 6, 2015.

23. Kaipa, C. S. R., A. B. Yakovlev, S. I. Maslovski, and M. G. Silveirinha, "Mushroom-type high-impedance surface with loaded vias: Homogenization model and ultra-thin design," *IEEE Antennas and Wireless Propagation Letters*, Vol. 10, 1503–1506, 2011.